Dimensional quantization and zero-field spin splitting of holes in GaAs nanowires

I. A. Kokurin *
National Research Ogarev Mordovia State University, 430005 Saransk, Russia
and Ioffe Institute, 194021 St. Petersburg, Russia

(Received 4 May 2023; revised 12 September 2023; accepted 20 September 2023; published 6 October 2023)

Nanowires (NWs) of III-V semiconductor materials have been of interest to researchers for the last two decades. Knowledge of the subband spectrum of charge carriers in NWs and NW-based structures is very important for current applications. The electronic subband spectrum in NWs is currently known in detail, while for holes it is found with significant simplifications. One or more of the following crucial features are usually neglected: the real NW cross section shape, the crystal orientation of the NW, an accounting for the real anisotropic Hamiltonian of the bulk host material, and contributions that are due to the lack of an inversion center in the crystal lattice. Here we present a detailed calculation of hole subbands in GaAs NWs with the [111] orientation with a zinc blende crystal lattice, taking into account all the above four features. The spectrum of hole subbands based on the 4×4 Luttinger Hamiltonian is numerically calculated taking into account two main contributions arising from the lack of inversion symmetry (the T_d point group) in the lattice of the host crystal. Accounting for these contributions leads to the appearance of spin splitting only for some subbands, in accordance with symmetry considerations. However, a significant rearrangement also occurs in the spectrum of nonsplit subbands. The hole densities are visualized, and it is shown that the contribution of terms with T_d symmetry significantly changes the structure of the multicomponent wave function. Thus, taking into account the lack of an inversion center is essential for the spectrum of hole subbands and wave functions in GaAs NWs. This can be more pronounced for NWs of III-V materials constituted by heavy elements, such as InSb, where spin-orbit interaction is stronger. The effect of a transverse electric field leading to so-called Rashba spin splitting is considered as well.

DOI: 10.1103/PhysRevB.108.165301

I. INTRODUCTION

Nanowires (NWs) of semiconductor materials of the $A^{III}B^{V}$ group are of great interest due to a wide range of possible applications, as well as compatibility with existing silicon technology [1]. Here we mean not only homogeneous NWs, but also the so-called radial heterostructures, also known as core-shell structures. NWs are currently used as the main element of field-effect transistors [2,3], photodetectors [4] (see also the review in Ref. [5] and references therein), and piezoelectric nanogenerators [6]. NWs are also widely used in the creation of such devices as light-emitting diodes, chemical and gas sensors, waveguides, solar cells, and optical converters [7]. The possible applications of NWs in photovoltaics, thermoelectrics, and betavoltaics have recently been outlined in Ref. [8].

In recent years, many low-dimensional systems, including NW-based structures, have found their application in the field of quantum computation. When creating semiconductor qubits [9], it turns out that, for a number of reasons, it is more convenient to use the hole spin [10–12], rather than electron one for information storage. Recently, various implementations of hole-spin qubits have been proposed [13–15], including using NW-based structures. In this context, it is of interest to consider zero-field spin splittings of valence subbands in NWs. It should be noted that significant theoretical progress has been made in the direction of the zero-field spin splitting calculation of conduction subbands in NWs [16–25].

At the same time, the zero-field spin splitting of hole subbands in NWs has not been studied in such detail. There are $\mathbf{k} \cdot \mathbf{p}$-based theoretical works devoted to the spin splitting of hole subbands in NWs [26–28]. However, in the above works, only the Rashba spin splitting mechanism [29] caused by structure inversion asymmetry (SIA) was taken into account. An atomistic calculation [30] indicates the transition of the hole Rashba effect in NWs from strong field dependence to saturation, in contrast to an electron behavior. Another mechanism, known as the Dresselhaus spin splitting [31], is due to the lack of an inversion center in the lattice of the host semiconductor material (bulk inversion asymmetry, BIA). For NWs of semiconductor materials with the diamond crystal lattice, such as Si and Ge (see Refs. [26–28]), which have inversion symmetry, there is no Dresselhaus splitting. However, for NWs with a zinc blende (ZB) or wurtzite (WZ) lattice (e.g., from semiconductors of the $A^{III}B^{V}$ group), such splitting takes place. The atomistic calculation and symmetry consideration [32] show that BIA-induced spin splitting in NWs with a ZB crystal lattice crucially depends on crystal orientation: In particular, for a [111]-oriented NW, there is no Dresselhaus spin splitting for electrons; in contrast, for certain hole subbands it takes place, but for others it is equal to zero.

*ivan.a.kokurin@gmail.com

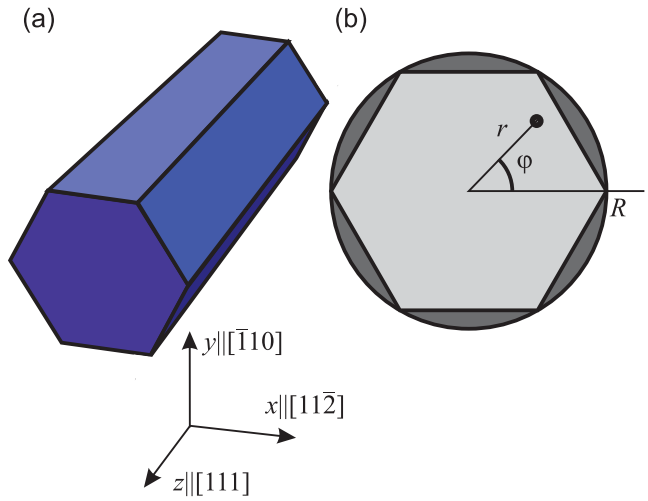

FIG. 1. (a) Sketch of a NW with a hexagonal cross section. The axes of the coordinate system are indicated. (b) The use of a circular basis set: The shaded areas between the circle and the hexagon correspond to nonzero values of the "hexagonality potential" $V(r, \varphi)$.

At the same time, as far as we know, there is no information in the literature about the $\mathbf{k} \cdot \mathbf{p}$ calculation of the Dresselhaus spin splitting of hole subbands in NWs.

Due to the large surface-to-volume ratio, the lattice mismatch strain in NWs can be elastically relaxed at the NW free surface without dislocations. This can be used to grow heterostructures and III-V NWs directly on cheap substrates, such as Si, rather than lattice-matched but more expensive III-V substrates. The bulk GaAs is crystallized with a ZB crystal lattice. However, depending on the growth conditions and on the diameter, NWs can crystalize both with a ZB lattice and with a WZ lattice. Epitaxially grown III-V NWs with a ZB lattice are usually oriented along the [111] crystallographic direction and, for this reason, have a hexagonal cross section [see Fig. 1(a)]. Moreover, the axial polytypic ZB/WZ heterostructures can be realized [33]. It has been shown that it is possible to control the crystal structure of III-V NWs during growth [34] and even obtain periodic structures such as polytypic superlattices.

Detailed information about the subband spectrum of carriers (electrons and holes) in NWs is necessary to understand all the processes occurring in NWs and NW-based hybrid structures. There are first-principles methods [35,36] which, together with tight-binding calculations [37,38], give good accuracy in subband spectrum calculation, but they lose in clarity. Clarity is typical for the $\mathbf{k} \cdot \mathbf{p}$ method, which, even utilizing numerical diagonalization, makes it possible to trace the contribution of certain bands. This is the reason for the wide use of the $\mathbf{k} \cdot \mathbf{p}$ method in calculating the spectrum of carriers in semiconductor structures.

The electronic properties of NWs, including spin ones, have been intensively studied in the last two decades, while holes in NWs have been studied much less. In this context there are four key issues that are often not taken into account in $\mathbf{k} \cdot \mathbf{p}$ calculations. (i) The first issue is the real crystal orientation of NWs [39,40]. This is important for holes, which have a strongly anisotropic spectrum in many materials. (ii) The second issue is the real shape of the cross section. Frequently, in $\mathbf{k} \cdot \mathbf{p}$ calculations one considers the shape of the section to be circular or square [39–41]. (iii) The third issue is the use of a simple isotropic (or so-called spherical) approximation for the hole Hamiltonian in materials with T_d or O_h point symmetry. It should be recalled here that the spherical approximation gives an incorrect result even for subband extrema (at $k = 0$) both in quantum wells and in NWs. This issue is closely related to the issue described in the first point. (iv) The fourth issue is the lack of an inversion center in III-V crystals with a ZB lattice (point group T_d) and the fact that the related spin splittings, having both relativistic and nonrelativistic character, are neglected.

The first three issues are more or less currently closed in the literature, whereas the fourth is not discussed to the best of our knowledge. In this paper we will try to eliminate this shortcoming and will show that accounting for the inversion asymmetry is crucial and that inclusion of appropriate terms in the hole Hamiltonian leads to dramatic rearrangement of the subband spectrum and spatial behavior of the hole wave function.

It should also be noted that different mesh methods (finite difference and finite element methods) have been used for the calculation of the carrier subband spectrum in NWs [20,42,43]. The main disadvantage of such methods is the frequent appearance of rapidly oscillating nonphysical solutions for the envelope wave functions. Knowledge of the wave function on a discrete grid is also not always convenient, e.g., when calculating any observable quantity.

The aim of this work is to calculate the spectrum of hole subbands and the corresponding wave functions in homogeneous NWs of an $A^{III}B^{V}$ material (undoped or slightly p doped) with a ZB lattice. The real geometry (cross section shape and crystal orientation) of the NWs and the exact structure of the valence band of the host semiconductor material, including the effect of the lack of an inversion center, are taken into account. The effect of the transverse electric field leading to additional Rashba-type spin splitting is considered as well.

The paper is organized as follows. In Sec. II we consider a model and the Hamiltonian for holes in NWs with hexagonal cross section. The results of numerical diagonalization as well as the spin expectation values are presented in Sec. III. The hole probability densities, including the partial contributions of heavy holes (HHs) and light holes (LHs), are visualized. The effective masses in one-dimensional (1D) subbands are calculated as well. In Sec. IV, two main terms are included in the Hamiltonian to take into account the lack of an inversion center in the ZB lattice, which is important for holes in the valence band. Rashba-type spin splitting due to the transverse electric field is also considered. In Sec. V the obtained results are discussed and summarized. Calculation details are presented in Appendixes A and B.

II. MODEL AND HAMILTONIAN

Most semiconductors with a diamond and ZB crystal structure have the top of the valence band at the Γ point of the Brillouin zone. The Luttinger Hamiltonian [44] is a good approximation in order to describe the Γ_8 valence band structure

in semiconductors having a wide band gap E_g and the valence band spin-orbit splitting Δ [45]. In an invariant form, it is given by

$$\mathcal{H}_L = \frac{\hbar^2}{2m_0}\left[\left(\gamma_1 + \frac{5}{2}\gamma_2\right)\mathbf{k}^2 J_0 - 2\gamma_2(\mathbf{Jk})^2 + 2(\gamma_3 - \gamma_2)\sum_{i\neq j}(J_i k_i)(J_j k_j)\right], \tag{1}$$

where $\mathbf{J} = (J_x, J_y, J_z)$ is the vector of the 3/2 angular momentum matrices; J_0 is the unit 4×4 matrix; $\mathbf{k} = (k_x, k_y, k_z)$, with $\mathbf{p} = \hbar\mathbf{k}$ being the momentum operator; γ_i $(i = 1, 2, 3)$ are the Luttinger parameters, characterizing the valence band of a bulk material; and m_0 is the free electron mass. This Hamiltonian is written in the principal cubic axes: $x||[100]$, $y||[010]$, $z||[001]$.

An explicit form of the Hamiltonian depends on the choice of basis functions. Here the so-called canonical basis $|3/2, J_z\rangle$ (with the standard choice of Clebsch-Gordan coefficient phases) is used, which is characterized by the z projection of the hole spin: $J_z = \pm 1/2, \pm 3/2$. The explicit form of basis functions and corresponding angular momentum matrices can be found, for instance, in Refs. [46,47].

Using the coordinate transformation (see Appendix A), one can rewrite the Hamiltonian in the new reference frame. The details of the coordinate transformation for the Luttinger Hamiltonian can be found in Ref. [27]. In the new axes, $x||[11\bar{2}]$, $y||[\bar{1}10]$, $z||[111]$, the Luttinger Hamiltonian is given by (see also, for instance, Ref. [48])

$$\mathcal{H}_L^{[111]} = \begin{pmatrix} F & H & I & 0 \\ H^* & G & 0 & I \\ I^* & 0 & G & -H \\ 0 & I^* & -H^* & F \end{pmatrix}, \tag{2}$$

with

$$F = \frac{\hbar^2}{2m_0}\left[(\gamma_1 + \gamma_3)\left(k_x^2 + k_y^2\right) + (\gamma_1 - 2\gamma_3)k^2\right],$$

$$G = \frac{\hbar^2}{2m_0}\left[(\gamma_1 - \gamma_3)\left(k_x^2 + k_y^2\right) + (\gamma_1 + 2\gamma_3)k^2\right],$$

$$H = -\frac{\hbar^2}{2m_0}\left[\sqrt{\frac{2}{3}}(\gamma_3 - \gamma_2)k_+^2 + \frac{2}{\sqrt{3}}(2\gamma_2 + \gamma_3)kk_-\right],$$

$$I = -\frac{\hbar^2}{2m_0}\left[\frac{1}{\sqrt{3}}(\gamma_2 + 2\gamma_3)k_-^2 + 2\sqrt{\frac{2}{3}}(\gamma_3 - \gamma_2)kk_+\right],$$

where $k_\pm = k_x \pm ik_y$. Here, the momentum operator k_z is replaced by its eigenvalue k due to the translational invariance of the problem in the direction z. The order of the basis functions in (2) is as follows: $J_z = +3/2, +1/2, -1/2, -3/2$.

We will consider a hole confined in a NW with a hexagonal cross section. The spectral problem evidently cannot be solved exactly. Recently, a similar problem for electrons with scalar effective mass was numerically solved [49]. Here, this method is generalized to the case of a complex valence band.

The following composite basis functions [Bloch functions multiplied by envelope functions, which are written in cylindrical coordinates (r, φ, z)] are used:

$$|J_z; m, n; k\rangle = |3/2, J_z\rangle \frac{\sqrt{2}}{RJ_{|m|+1}(j_{mn})} J_{|m|}\left(j_{mn}\frac{r}{R}\right) \times \frac{1}{\sqrt{2\pi}} e^{im\varphi} \frac{1}{\sqrt{L}} e^{ikz}, \tag{3}$$

which are eigenstates of the simplified Luttinger Hamiltonian [all off-diagonal matrix elements in Eq. (2) are omitted] with an additional hard-wall confinement on a cylinder of radius R. Thus these functions are eigenfunctions of the hole inside the cylindrical NW described by the simplified Hamiltonian. Here, $J_m(x)$ is the Bessel function of the first kind of order m, and j_{mn} is the nth zero of $J_m(x)$; $m = 0, \pm 1, \pm 2, \ldots$ and $n = 1, 2, \ldots$.

The eigenenergies $E_{mn}^{J_z}(k)$ corresponding to the above basis functions are given by [50]

$$\frac{E_{mn}^{\pm 3/2}(k)}{E_0} = (\gamma_1 + \gamma_3)j_{mn}^2 + (\gamma_1 - 2\gamma_3)(kR)^2, \tag{4}$$

$$\frac{E_{mn}^{\pm 1/2}(k)}{E_0} = (\gamma_1 - \gamma_3)j_{mn}^2 + (\gamma_1 + 2\gamma_3)(kR)^2, \tag{5}$$

where $E_0 = \hbar^2/2m_0R^2$.

Using such a composite basis, one can calculate the matrix elements of the Luttinger Hamiltonian (2) that are off-diagonal in the hole spin. The subsequent numerical diagonalization of the obtained Hamiltonian matrix yields the subband energies and wave functions of holes in a cylindrical NW. Two points should be noted here. First, numerical diagonalization is impossible for a matrix of infinite size. This means that we must truncate the Hamiltonian matrix to a size that provides the required diagonalization accuracy. Second, for holes in NWs, the transverse and longitudinal motions are not separated. However, because of the translational invariance, the longitudinal momentum is a good quantum number, and for this reason k enters the Hamiltonian matrix as a parameter. This, in turn, means that in order to find the spectrum of hole subbands, we have to diagonalize the Hamiltonian matrix for a certain number of fixed k.

Here, we are interested in the hole states in NWs with a hexagonal cross section. To consider the real hexagonal cross section, it is necessary to add a special potential, which takes into account the difference between a circular section and a hexagonal one for the case of a hexagon inscribed in a circle [49] [see Fig. 1(b)]. Obviously, the additional potential will have matrix elements diagonal in the hole spin J_z, while the basis functions with different quantum numbers m and n can be mixed by this potential. The longitudinal momentum k remains a good quantum number in the hexagonal NW as well.

The "hexagonality potential" $V(r, \varphi)$ is chosen to be equal to zero inside the hexagon and has a finite magnitude V_0 in areas which are inside the circle but at the same time are outside the hexagon [see Fig. 1(b)]. We cannot technically set V_0 to equal infinity in order to provide zero boundary conditions at the hexagon. However, within the $\mathbf{k} \cdot \mathbf{p}$ approximation any high V_0 value, say, 1 eV or higher, is effectively infinite. In this case the wave function will not penetrate significantly into the barrier areas.

It should be noted that there are other possibilities for choosing a basis set. In Ref. [49], for example, two bases were used: (i) a circular basis like the one used here and (ii) a rectangular one. In the latter case, a regular hexagon is inscribed in a rectangle of $2R \times \sqrt{3}R$ size. The use of such a basis allows one to find exactly the matrix elements of the hexagonality potential. However, from the symmetry point of view, it is convenient to use a basis in which the rotational symmetry is higher than a hexagonal one (C_6 axis). Some subbands of the hexagonal NW, which should be degenerate, will have slightly different energies after numerical diagonalization of the truncated Hamiltonian matrix if a rectangular basis is used. Thus the use of a low-symmetry basis requires more basis functions to provide the same accuracy. For this reason, here we restrict ourselves to using only the circular basis.

The spectral problem is reduced to finding the eigenvalues and eigenvectors of the Hamiltonian matrix $\mathcal{H} = \mathcal{H}_L^{[111]} + V(r, \varphi)J_0$ written in the basis (3). To write the Luttinger Hamiltonian (2) in the basis (3), it is necessary to know the matrix elements of the operators $k_\pm$ and $k_\pm^2$ between the transverse envelopes $|mn\rangle$, which are part of complete basis functions (3). These matrix elements $\langle m'n'|k_\pm^l|mn\rangle$ $(l = 1, 2)$ are presented in Appendix B. The matrix elements of the hexagonality potential $\langle J_z;' m'n'; k'|V(r, \varphi)|J_z; mn; k\rangle$ are proportional to the overlap integral $I_{m'n';mn}$ of basis functions in a single barrier segment (one of six). One can use some symmetry arguments to calculate the matrix elements. They are given by

$$\langle m'n'|V(r, \varphi)|mn\rangle = 6V_0\delta_{m',m+6M}I_{m'n';mn}, \tag{6}$$

where $M = 0, \pm1, \pm2, \ldots$. These matrix elements obviously do not depend on J_z and k and are diagonal with respect to them. An explicit form of the overlap integral is presented in Appendix B, and it can be found numerically.

III. NUMERICAL DIAGONALIZATION

For numerical diagonalization, we must truncate the size of the found Hamiltonian matrix and work with a matrix of finite size. We use the following procedure: We restrict ourselves to the threshold energy $E_{th} = 4000E_0$ and take into account only the basis functions whose eigenenergies for $k = 0$ are less than E_{th}. For GaAs band parameters [47] ($\gamma_1 = 6.85$, $\gamma_2 = 2.10$, $\gamma_3 = 2.90$) this corresponds to the number $N = 660$ of basis functions, of which $N_h = 184$ are of HH and $N_l = 476$ of LH character. The value $V_0 = 4000E_0$ is used as well.

The energy spectrum obtained by the numerical diagonalization of the truncated Hamiltonian matrix is shown in Fig. 2. These results are valid for GaAs NWs of any radius. In the particular case of a NW with $R = 10$ nm we have

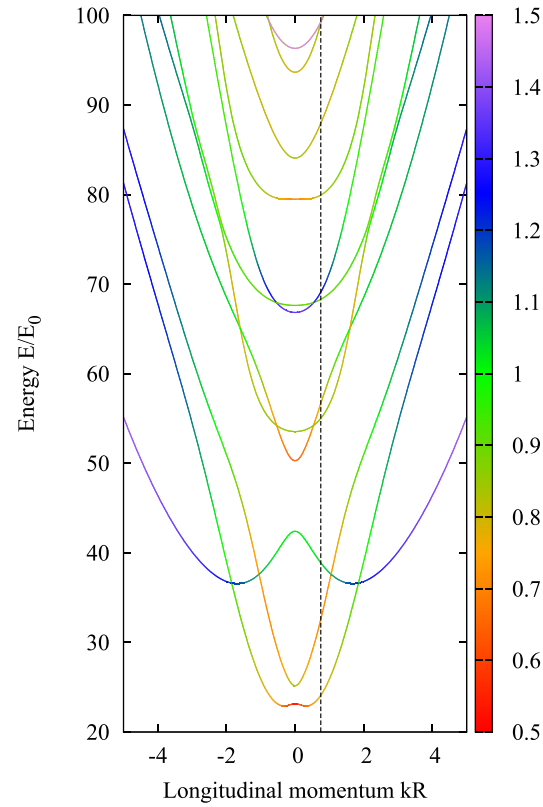

FIG. 2. The hole subband energy spectrum of GaAs NW ($\gamma_1 = 6.85$, $\gamma_2 = 2.10$, $\gamma_3 = 2.90$). The parameters of the numerical diagonalization are as follows: $E_{th} = V_0 = 4000E_0$. The energy is scaled to E_0. The colors reflect the HH and LH contributions to the multicomponent wave function. The magnitude $\sqrt{\langle J_z^2\rangle_i(k)}$ is calculated for the ith subband by means of Eq. (9). It takes values in the interval $(\frac{1}{2}; \frac{3}{2})$; see color bar. The crossings of subbands with the vertical dashed line correspond to the states whose wave functions are visualized in Fig. 4.

$E_0 = 0.38$ meV, which corresponds to $E_{th} = V_0 = 1.52$ eV. The results can be easily rescaled for NWs of any radius R. It should be noted that all hole subbands are doubly degenerate. This is a consequence of the simultaneous presence of time-reversal symmetry (TRS) and symmetry with respect to spatial inversion. It should be remembered that the Luttinger Hamiltonian used, as well as the hexagonality potential, is invariant under spatial inversion. Calculations for NWs taking into account the lack of an inversion center in a material with a ZB lattice (point group T_d) are presented in Sec. IV.

The numerical diagonalization also yields for the ith subband the expansion coefficients $C^i_{J_z;mn}(k)$ with respect to the basis (3). Thus the spatial behavior of the subband wave function

$$|i; k\rangle = \sum_{J_z mn} C^i_{J_z;mn}(k)|J_z; mn; k\rangle \tag{7}$$

can be studied.

The quantum-mechanical density matrix $\rho^i_{\alpha'\alpha}(k) = C^{i*}_{\alpha'}(k)C^i_\alpha(k)$ can be used to find the mean value of any observable A in the state $|i; k\rangle$

$$\langle A\rangle_i(k) = \mathrm{Tr}[A\rho^i(k)]. \tag{8}$$

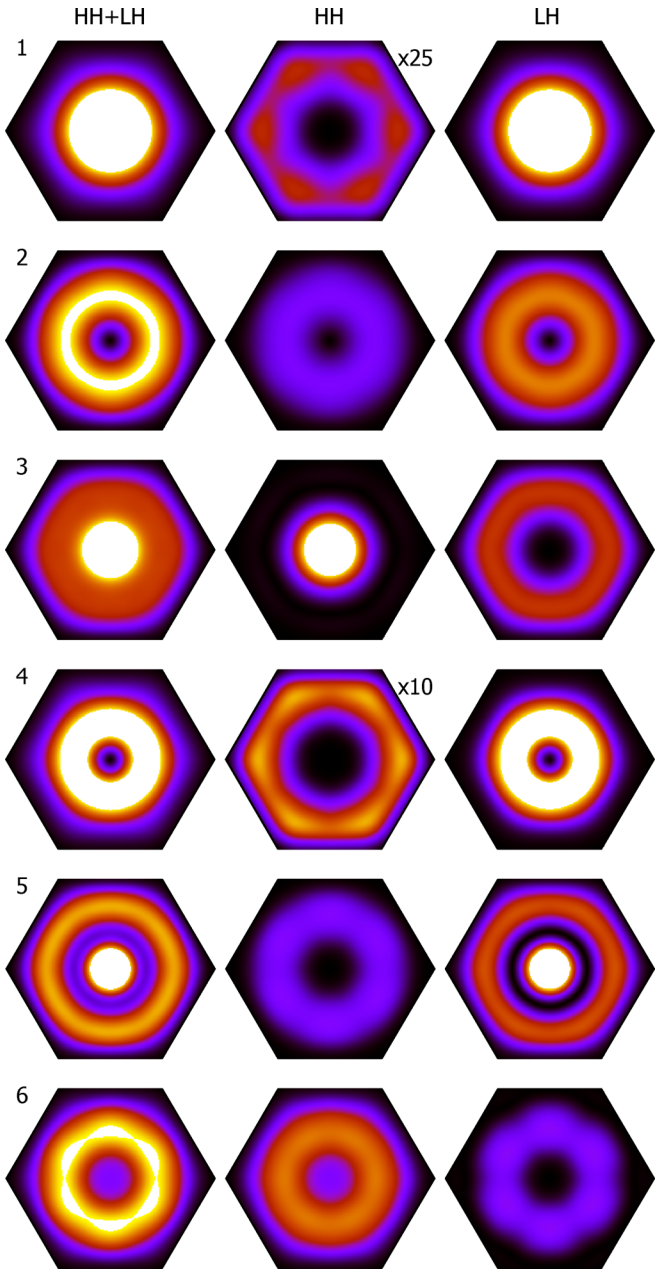

FIG. 3. The transverse hole density maps $|\Psi(r,\varphi)|^2$ for GaAs NW at $k=0$ ($\gamma_1=6.85$, $\gamma_2=2.10$, $\gamma_3=2.90$). The separate contributions for HH and LH are also depicted. The maps are in arbitrary units, but all $|\Psi|^2$ are normalized to the same value. For the first and fourth subbands the HH contributions of the hole density are rescaled for clarity: They are increased by 25 and 10 times, respectively.

In order to trace the spin structure of hole subbands (the relative contributions of HHs and LHs to the wave function), the mean values of the $J_z^2=\mathrm{diag}\{9/4,\,1/4,\,1/4,\,9/4\}$ operator can be calculated using Eq. (8). Since the J_z^2 operator is diagonal in the hole spin, its mean values can be rewritten in a simpler form using the expansion coefficients:

$$\left\langle J_z^2\right\rangle_i(k)=\sum_{J_z=\pm1/2,\pm3/2}J_z^2\sum_{mn}\left|C^i_{J_z;mn}(k)\right|^2. \tag{9}$$

TABLE I. The effective masses of 1D hole subbands. For subbands with more than one extremum, the effective mass in the side extrema is presented in the third column indicating the position of the extremum.

No.	m^*/m_0 at $k=0$	m^*/m_0 at $k\neq0$
1	−0.142	0.175 ($kR=\pm0.315$)
2	0.044	
3	−0.077	0.405 ($kR=\pm1.682$)
4	0.056	
5	0.472	
6	0.287	
7	0.965	

The square root of this value is plotted in Fig. 2 using a color scale. It can be seen that most of the subbands have a predominant LH character near $k=0$, with an increasing contribution from HHs as k increases. An exception is the sixth subband, which at $k=0$ contains mainly the HH contribution.

The effective masses $(m_i^*)^{-1}=\partial^2E_i(k)/\partial(\hbar k)^2$ for low-lying subbands are calculated. For the first seven subbands they are presented in Table I. For subbands with more than one extremum (W-like shape) and negative effective mass at $k=0$, positive masses in side extrema are also presented with an indication of the position of these extrema.

The accuracy of the numerical procedure is estimated as follows. The overlap integrals are found numerically with an accuracy better than 10^{-4}. The diagonalization process has an accuracy of the same order. Thus the overall accuracy is mainly determined by the size of the truncated Hamiltonian matrix, i.e., the number of basis functions N or the truncation energy E_{th}. To evaluate the influence of the matrix size on the accuracy of the spectrum calculation in Fig. 2, we will do the following. Consider a numerical diagonalization of the Hamiltonian matrix with the same parameters (see the caption of Fig. 2), except for $E_{th}=3000E_0$ (which corresponds to $N=484$ with $N_h=134$ and $N_l=350$). In this case, the first 12 subbands (taking into account the Kramers degeneracy) have subband energies that exceed those shown in Fig. 2 by less than $0.90E_0$ over the entire range of k, which is almost indistinguishable in the scale of Fig. 2. On the other hand, an increase in the strength V_0 of the hexagonality potential leads to a slight increase in the subband energies, which is associated with a decrease in the penetration of the wave function into the "barrier" region. Thus, a simultaneous increase in E_{th} and V_0 does not lead to significant changes in the results of numerical diagonalization. We have approximately the same results for $E_{th}=V_0=3000E_0$ and $E_{th}=V_0=4000E_0$, with the latter requiring twice as much computation time. It should also be noted that the band parameters γ_i ($i=1,2,3$) are known with finite accuracy. This means that a slight change in the band parameters will have a stronger effect on the subband spectrum than a further increase in the size of the Hamiltonian matrix (the number of basis functions N or the truncation energy E_{th}).

The solution of the spectral problem includes finding the coefficients $C^i_{J_z;mn}(k)$. This means that the spatial behavior of the wave function (7) can be traced. The latter is a complex-

valued quantity. For this reason, the transverse hole density $|\Psi|^2$ is presented here. Since the transverse and longitudinal motions are not separated, the spatial behavior of the transverse function depends on the longitudinal momentum k. The transverse hole density in 1D subbands is depicted in Fig. 3 for a longitudinal momentum $k = 0$. The separate HH and LH contributions are presented as well. Here, one can see the confirmation of what is shown in Fig. 2 using a color scale: Most of the subbands near $k = 0$ have a main LH contribution, whereas the HH one is small. The exception is the third and sixth subbands: In the third subband the HH and LH contributions are of the same order, while in the sixth subband, the HH contribution dominates. It can be seen that in addition to states with a pronounced LH or HH character, there are specific states for which the HH and LH contributions to the multicomponent wave function are spatially separated. This concerns the third subband.

In Fig. 4 the transverse hole density maps are presented for the case of a nonzero longitudinal momentum, $kR = 0.75$. It should be noted that the numbering of the subbands corresponds to the increase in energy at given k. This means that this numbering may differ from the numbering for $k = 0$ (see Fig. 3) due to the possible crossings in the subband spectrum. The states whose wave functions are shown in Fig. 4 correspond to the crossings of the subband energies with the vertical dashed line in Fig. 2.

The patterns of Fig. 4 are significantly different from those in Fig. 3, which is due to the subband intermixing, as well as the crossings and anticrossings in the spectrum. The O_h symmetry of the Luttinger Hamiltonian (here the lack of an inversion center is not yet taken into account) is reduced by the NW's [111] orientation and quantum confinement to the D_{3d} point symmetry. The maps of Fig. 4 depict the hole density and its HH and LH components for one of two degenerate subbands only. These maps do not reflect the whole D_{3d} symmetry of the system. The use of the inversion operation $\boldsymbol{i}$ or reflection in diagonal symmetry planes $\boldsymbol{\sigma}_d$ (the {110} planes, which after projection onto the NW cross section look like the lines connecting opposite vertices of a hexagon) transforms the depicted hole densities into those for the corresponding degenerate state. Thus the total hole densities (as well as HH and LH components) after summation over degenerate states have the necessary D_{3d} point symmetry, as it should be. Finally, the presence of $3\boldsymbol{\sigma}_d$ and $3\boldsymbol{c}_2$ symmetry elements leads to C_6 rotational symmetry in the cross-sectional plane for hole density maps.

At the same time, density maps for $k = 0$ (see Fig. 3) have C_6 rotational symmetry for each member of the pair of degenerate states. On the one hand, this is a consequence of the C_∞ symmetry of the Luttinger Hamiltonian (2) at $k = 0$. In this case the C_6 symmetry is imposed by the hexagonality potential. On the other hand, the pair of degenerate states at $k = 0$ are additionally linked by TRS. The latter means that the hole densities for the degenerate states must coincide, i.e., the C_6 rotational symmetry holds not only for the total hole density, but also for the density in each of the degenerate states. It should be noted that the following restrictions are imposed on the quantum states by TRS: The time-reversed state ($k \to -k$ and $J_z \to -J_z$) is described by the complex-conjugated wave function; in our case, this concerns the corresponding components of the multicomponent envelope function $[\Psi_{J_z}(k) \to \Psi_{-J_z}(-k) = \Psi^*_{J_z}(k)]$.

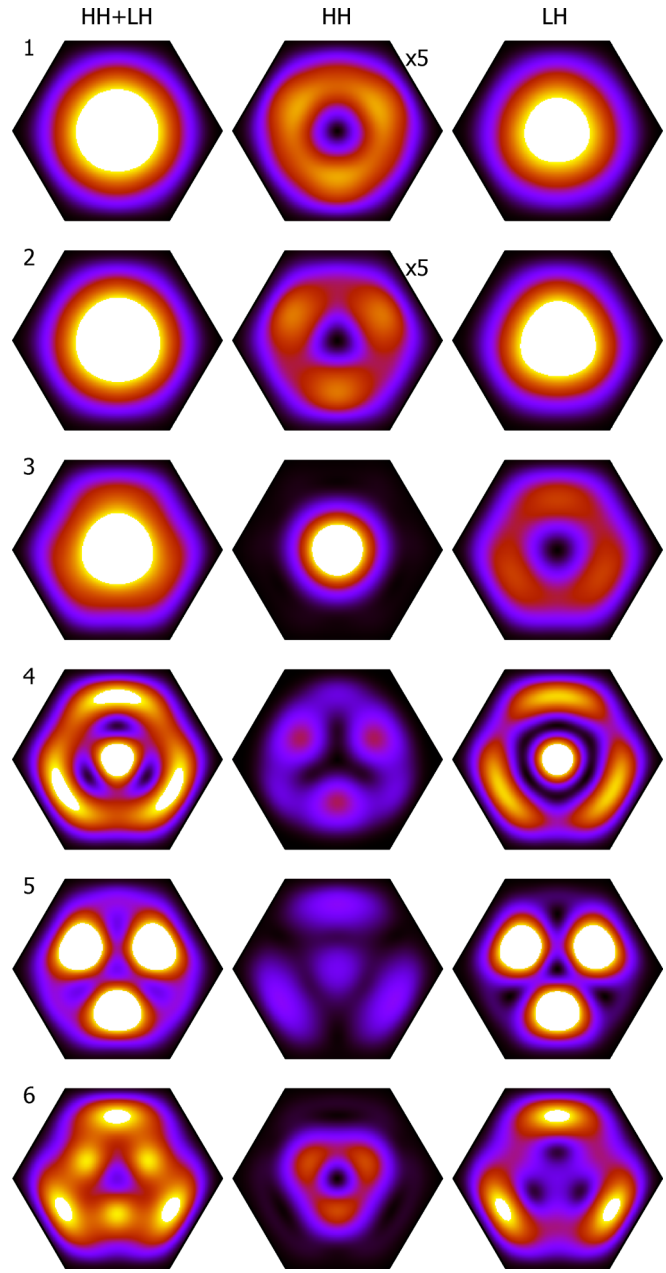

FIG. 4. The transverse hole density maps $|\Psi(r, \varphi)|^2$ for GaAs NW at $kR = 0.75$ ($\gamma_1 = 6.85$, $\gamma_2 = 2.10$, $\gamma_3 = 2.90$). The separate contributions for HH and LH are depicted. The maps are in arbitrary units, but all $|\Psi|^2$ are normalized to the same value. For the first and second subbands the HH contributions of the hole density are rescaled for clarity: They are increased by 5 times.

Note that when calculating the hole states in nanostructures, the so-called spherical approximation is often used (though this use is not always justified). This corresponds to the approximation $\gamma_2 = \gamma_3$ and does not take into account the last term in Eq. (1). This approximation not only cannot correctly describe the density maps in Fig. 4, which have a rotational symmetry of the third order, but also leads to incorrect subband energies at $k = 0$.

It should be noted that the accuracy of the calculation of $|\Psi|^2$ was also examined. There is no noticeable difference for the cases $E_{th} = 4000E_0$ (660 basis functions) and $E_{th} = 1000E_0$ (152 basis functions) both for the maps of Fig. 3 and for the maps of Fig. 4.

It can be seen that the results of Figs. 2 and 3 resemble the results of Ref. [51], where a similar problem was solved for GaAs/AlGaAs core-shell NW. This means that the structure studied in Ref. [51] has rather high barriers and the wave function does not penetrate them, which additionally justifies our use of the hexagonality potential model. In addition, the eight-band $\mathbf{k}\cdot\mathbf{p}$ model was used in Ref. [51], which is redundant for holes in GaAs. This is due to the fact that the band gap $E_g = 1.5$ eV and the spin-orbit splitting $\Delta = 0.35$ eV of the valence band significantly exceed the characteristic energy scales in the problem. Thus hole states in NWs of not-too-small radius, for which the envelope function approximation is still applicable, can be described in terms of the Luttinger Hamiltonian.

IV. ZERO-FIELD SPIN SPLITTING

There are two main types of zero-field spin splitting [52] and corresponding contributions into the electron or hole Hamiltonian in semiconductor structures. The first one, known as the Dresselhaus term [31], is due to the lack of an inversion center in the lattice of the host semiconductor material, BIA. The second one, known as the Rashba term [29], originates from SIA, i.e., is due to the lack of an inversion symmetry at the macroscopic level. In particular, Rashba splitting takes place in asymmetric heterostructures, which asymmetry can be caused by the growth conditions, the applied electric field, nonuniform doping, etc.

Zero-field spin splittings are very important for such effects as Dyakonov-Perel spin relaxation [53,54], photogalvanic effects [55], current-induced spin polarization (see, for instance, the brief overview in Ref. [56] and references therein), and related phenomena (spin Hall effect, inverse spin Hall effect, etc.).

The spin-orbit effects are more pronounced for the states of the valence band than for those of the conduction band. This is a consequence of the fact that the valence band is constituted by p-type states (angular momentum of 1) whereas the conduction band originates from s-type states (angular momentum of 0). Thus the spin splitting in the conduction band arises due to the $\mathbf{k}\cdot\mathbf{p}$ interaction with the valence and other bands and is weaker.

In Sec. IV A, the terms with T_d point symmetry are added to the bulk hole Hamiltonian to take into account the lack of an inversion center in the ZB lattice. The point group T_d has no inversion $\boldsymbol{i}$ among its elements, which means that the twofold degeneracy of the subband spectrum discussed in Sec. III can be (but will not necessarily be) lifted. The full Hamiltonian is numerically diagonalized, and the corresponding wave functions is visualized. Comparison with the results of Sec. III shows that it is important to take into account the real symmetry of the host semiconductor crystal. As a SIA source the transverse electric field is considered in Sec. IV B. Accounting for both contributions leads to a significant rearrangement of the spectrum of hole subbands and wave functions.

A. Dresselhaus spin splitting

The Dresselhaus spin term [31], caused by BIA, takes place for electrons and holes in bulk material as well as in low-dimensional structures. In the latter case, dimensional quantization renormalizes the Dresselhaus term, e.g., the splitting is proportional to k^3 [31] for electrons in the Γ_6 conduction band of a semiconductor with a ZB lattice, while in quantum wells of the same material the leading contribution is linear in k [54]. The zero-field spin splitting of holes in the Γ_8 band in bulk $A^{III}B^{V}$ semiconductors [57] is also well studied. In low-dimensional systems the spin splitting of holes was first studied by Rashba and Sherman [58] in a symmetric quantum well.

For holes of the Γ_8 band in the bulk material there are one linear-in-k and four cubic-in-k invariants [47,57,59]. The former one is given by

$$\mathcal{H}_1 = \frac{2}{\sqrt{3}} C_k \left[k_x \left\{ J_x, J_y^2 - J_z^2 \right\} + \text{c.p.} \right], \tag{10}$$

where $\{A, B\} = \frac{1}{2}(AB + BA)$ is the symmetrized product and c.p. stands for cyclic permutation. This operator is written in principal cubic axes. The explicit form of this operator, suitable for our consideration, after the coordinate transformation (see Appendix A) is given by

$$\mathcal{H}_1^{[111]} = \frac{2}{\sqrt{3}} C_k \begin{pmatrix} 0 & -\frac{i}{2}k_- & \frac{i}{2\sqrt{2}}k_+ & -i\sqrt{\frac{3}{2}}k \\ \frac{i}{2}k_+ & 0 & i\frac{\sqrt{3}}{2}k_- & -\frac{i}{2\sqrt{2}}k_+ \\ -\frac{i}{2\sqrt{2}}k_- & -i\frac{\sqrt{3}}{2}k_+ & 0 & -\frac{i}{2}k_- \\ i\sqrt{\frac{3}{2}}k & \frac{i}{2\sqrt{2}}k_- & \frac{i}{2}k_+ & 0 \end{pmatrix}. \tag{11}$$

Here, the operator k_z is again replaced by its eigenvalue k. It is well known that in a bulk material at $k||[111]$ the HH spectrum is split by this contribution, while the LH branch remains degenerate [60].

In GaAs, out of four invariants cubic in k, the following dominates (the rest have two-orders-of-magnitude smaller strength parameters [47]):

$$\mathcal{H}_3 = b_{41}^{8v8v} \left[J_x \left\{ k_x, k_y^2 - k_z^2 \right\} + \text{c.p.} \right], \tag{12}$$

which after coordinate transformation is given by

$$\mathcal{H}_3^{[111]} = b_{41}^{8v8v} \begin{pmatrix} H_{11} & H_{12} & 0 & 0 \\ H_{12}^* & \frac{1}{3}H_{11} & \frac{2}{\sqrt{3}}H_{12} & 0 \\ 0 & \frac{2}{\sqrt{3}}H_{12}^* & -\frac{1}{3}H_{11} & H_{12} \\ 0 & 0 & H_{12}^* & -H_{11} \end{pmatrix}, \tag{13}$$

where

$$H_{11} = -\frac{\sqrt{3}i}{4\sqrt{2}}(k_+^3 - k_-^3),$$

$$H_{12} = \frac{i}{4}[-k_+k_-^2 + \sqrt{2}k_+^2 k + 4k_-k^2].$$

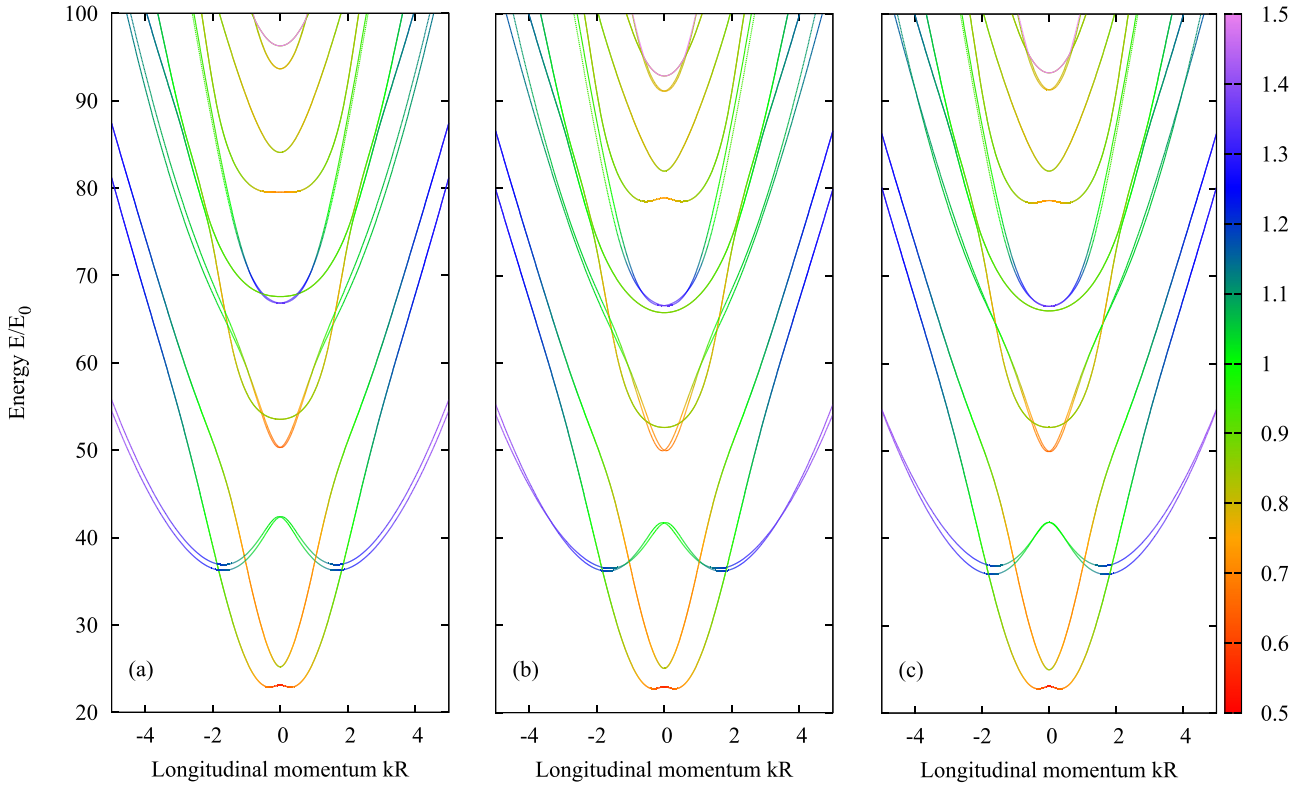

FIG. 5. Energy spectrum of the hole subbands of GaAs NW taking into account the lack of inversion symmetry ($\gamma_1 = 6.85$, $\gamma_2 = 2.10$, $\gamma_3 = 2.90$): (a) the k-linear contribution $\mathcal{H}_1^{[111]}$ is taken into account, $\frac{2C_k}{\sqrt{3}E_0R} = 0.103$; (b) the k-cubic contribution $\mathcal{H}_3^{[111]}$ is taken into account, $\frac{b_{41}^{8v8v}}{E_0R^3} = 0.216$; (c) both contributions $\mathcal{H}_1^{[111]}$ and $\mathcal{H}_3^{[111]}$ are taken into account for the same parameter magnitudes. The energy is scaled to E_0. The color reflects the HH and LH contributions to the multicomponent wave function. The magnitude $\sqrt{\langle J_z^2\rangle_i(k)}$ is calculated for the ith subband by means of Eq. (9). It takes values in the interval $(\frac{1}{2};\frac{3}{2})$; see color bar.

The matrix elements of the operators $k_+^p k_-^q$ calculated between the transverse envelopes $|mn\rangle$ of the basis functions (3) are presented in Appendix B. After substituting them into Eq. (13) it is easy to see that this operator is non-Hermitian. This problem is close to that which arose when considering zero-field spin splittings of holes in quantum wells. It is possible that this problem (non-Hermiticity of the Hamiltonian) has previously become an obstacle in the study of the zero-field spin splitting of holes in NWs. There is no way to eliminate non-Hermiticity problems when you solve the Schrödinger equation on a grid. However, in our case, there is an easy way to avoid this difficulty. This is an additional forced symmetrization of the obtained matrix [61], i.e., replacement of matrix elements $\langle J_z'; m'n'; k|\mathcal{H}_3^{[111]}|J_z; mn; k\rangle$ by

$$\begin{aligned}\langle J_z'; m'n'; k|\mathcal{H}_3^{[111]}|J_z; mn; k\rangle_{\rm sym} \\ = \tfrac{1}{2}\langle J_z'; m'n'; k|\mathcal{H}_3^{[111]}|J_z; mn; k\rangle \\ + \tfrac{1}{2}\langle J_z; mn; k|\mathcal{H}_3^{[111]}|J_z'; m'n'; k\rangle^*. \end{aligned} \quad (14)$$

The total hole Hamiltonian, taking into account terms of Eqs. (11) and (13) and additionally symmetrized, can be numerically diagonalized. The result of numerical diagonalization is shown in Fig. 5. Here three different situations are considered for comparison. In Fig. 5(a) only the contribution (11) linear in k is taken into account. In Fig. 5(b) only the k-cubic contribution (13) is considered. Finally, both contributions are taken into account in the Hamiltonian, the result of which diagonalization is shown in Fig. 5(c).

The typical GaAs parameters are used [47]: $C_k = 3.4$ meV Å, $b_{41}^{8v8v} = 81.93$ eV Å^3. Figure 5 formally can be rescaled to different R. However, the spin splitting parameters deprive us of such freedom, because they must scale proportionally to each other. Thus Fig. 5 actually corresponds to NW with $R = 10$ nm ($E_0 = 0.38$ meV, $\frac{2C_k}{\sqrt{3}E_0R} = 0.103$, $\frac{b_{41}^{8v8v}}{E_0R^3} = 0.216$). At this NW radius, both contributions to the zero-field spin splitting are of the same order. As the NW radius decreases, the k^3 contribution (13) dominates.

It should be noted that the energy spectra of the subbands in Figs. 5(a) and 5(b), taking into account the terms $\mathcal{H}_1^{[111]}$ and $\mathcal{H}_3^{[111]}$ separately, do not depend on the sign of the corresponding parameter, C_k or b_{41}^{8v8v}, respectively. However, the relative sign of C_k and b_{41}^{8v8v} is important when both contributions are taken into account. Both positive (or both negative) values of these parameters [47] are used, since this combination ensures that the sign of the HH splitting in bulk GaAs is reversed in the [110] direction [62].

Our results agree with the symmetry analysis and atomistic calculations of Ref. [32]: In [111]-oriented NWs (C_{3v} symmetry) the Dresselhaus spin splitting does not take place for all

subbands. The spin degeneracy is lifted in the band if the corresponding double group representation is one-dimensional. If the double group representation has a dimension greater than one (typically two), then there is a degeneracy. In the case of the group C_{3v} there are both one- and two-dimensional irreducible representations.

It should be noted that not only does taking into account the terms (11) and (13) lead to the spin splitting of certain subbands, but also these terms influence the shape of the nonsplit subbands. In particular, one can compare the eighth pair of subbands in Fig. 2 with Figs. 5(b) and 5(c): For this pair of subbands, the simple close-to-parabolic shape is changed into a W-like one, having three extrema. This is due to the presence of nonzero k-independent matrix elements of $\mathcal{H}_3^{[111]}$.

Moreover, the wave functions and hole density maps (see Fig. 6) change significantly when $\mathcal{H}_1^{[111]}$ and $\mathcal{H}_3^{[1\bar{1}1]}$ terms are taken into account. These contributions restore the real third-order rotational symmetry of the density maps even at $k = 0$ (cf. Fig. 3).

B. Rashba spin splitting

The Rashba spin splitting [29] is associated with SIA. Our understanding of Rashba spin splitting goes back to works on the energy bands of semiconductors with a WZ crystal structure [63,64], and this splitting takes place in semiconductors without an inversion center that have a high-order symmetry axis (not lower than the third order). For example, in semiconductors with a WZ lattice, such splittings occur at k directed perpendicular to the hexagonal axis.

In two-dimensional systems (heterostructures, quantum wells), the Rashba splitting is a consequence of the asymmetry of the heteropotential. This can be achieved by growth conditions (different heights of barriers), nonuniform doping of barriers, etc. In addition, the Rashba spin splitting can be caused and continuously tuned using an external gate [65]. The latter can also be applied to NWs [66–68], which are used as an element of a field-effect transistor. In this context, NWs can also be adapted to the spin field-effect transistor proposed by Datta and Das [69].

We consider a homogeneous undoped NW. This means that the Rashba splitting can only be achieved by applying a transverse electric field. Now there are different gate geometries for NWs. The so-called wrapping (or gate-all-around) gates [70,71] or Ω-like gates [72] are used for suspended NWs or NW on a substrate, respectively. Nevertheless, the calculation of the electrostatic potential created in a hexagonal NW by such gates is in itself a difficult problem that deserves separate consideration. Here the simple case of a homogeneous transverse electric field $\mathbf{F}$ is considered. This can be realized when a NW is placed between the plates of a flat capacitor and the empty space is filled by an insulator (which may be a liquid) with the dielectric constant close in magnitude to that of the NW material.

The hexagonal symmetry of NWs implies that the spin splitting and the subband spectrum will depend on the orientation of the transverse electric field relative to the hexagonal cross section, which is determined by the angle φ_0 (measured from the x axis; see Fig. 1):

$$\mathbf{F} = (F\cos\varphi_0, F\sin\varphi_0, 0).$$

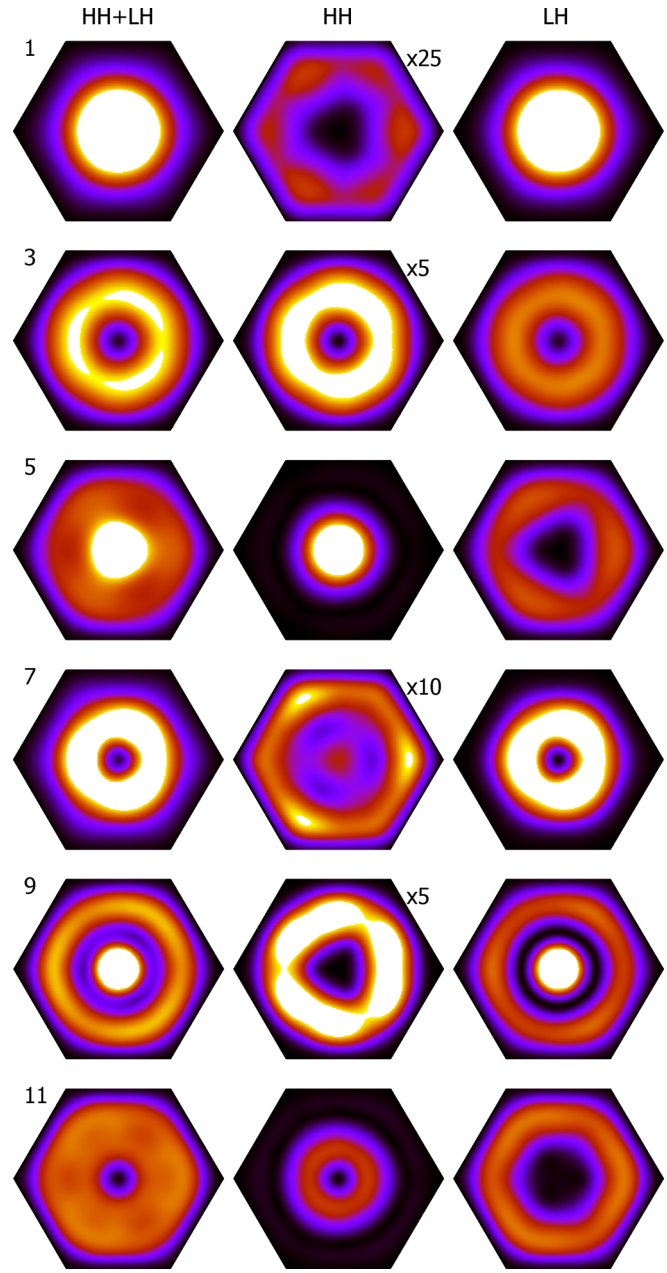

FIG. 6. The transverse hole density maps $|\Psi(r,\varphi)|^2$ for GaAs NW taking into account BIA terms (11) and (13) and corresponding to Fig. 5(c) at $k = 0$. The separate contributions for HH and LH are depicted. The maps are in arbitrary units, but all $|\Psi|^2$ are normalized to the same value. For some subbands the HH contributions of the hole density are rescaled for clarity: They are increased by 5, 10, or 25 times.

The potential energy of a hole placed in a uniform electric field in cylindrical coordinates is given by

$$\mathcal{H}_F = -eFr\cos(\varphi - \varphi_0). \tag{15}$$

Here, e is the absolute value of the electron charge.

In our considerations, it is important that the condition $eFR \ll V_0$ be fulfilled, i.e., the asymmetry of the total potential due to the electric field must be much smaller than the hexagonality potential. Otherwise, our concept of the

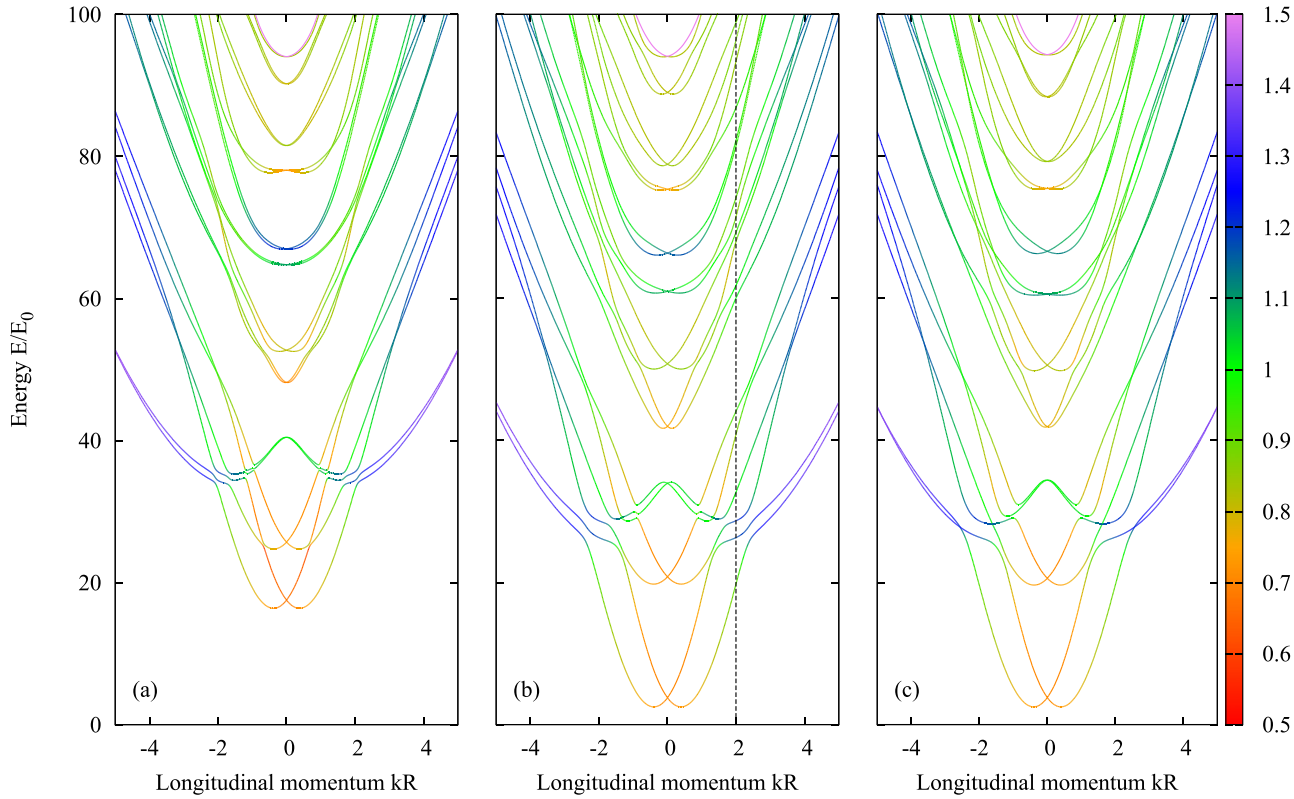

FIG. 7. The hole subband energy spectrum of GaAs NW in transverse electric field ($\gamma_1 = 6.85$, $\gamma_2 = 2.10$, $\gamma_3 = 2.90$, $\frac{2C_k}{\sqrt{3}E_0R} = 0.103$, $\frac{b_{41}^{8v8v}}{E_0R^3} = 0.216$). (a) $eFR/E_0 = 30$, $\varphi_0 = \pi/2$; (b) $eFR/E_0 = 70$, $\varphi_0 = \pi/2$; (c) $eFR/E_0 = 70$, $\varphi_0 = 0$. The energy is scaled to E_0. The color reflects the HH and LH contributions to the multicomponent wave function. The magnitude $\sqrt{\langle J_z^2\rangle_i(k)}$ is calculated for the ith subband by means of Eq. (9). It takes values in the interval $(\frac{1}{2}; \frac{3}{2})$; see color bar. The crossings of subbands with the vertical dashed line correspond to the states whose wave functions are visualized in Fig. 8.

hexagonality potential does not work, and the hole wave function may be nonzero in some of the shaded segments in Fig. 1(b). This condition imposes a limitation on the maximum magnitude of the electric field. The simple estimates show the following: For NW with $R = 10$ nm we have $E_0 = 0.38$ meV, and the electric field energies $eFR = 30E_0$ and $eFR = 70E_0$ correspond to moderate electric fields $F = 1.14 \times 10^4$ V/cm and $F = 2.66 \times 10^4$ V/cm, respectively. Thus, for the value $V_0 = 4000E_0$ used in the numerical calculation, the above condition is fulfilled.

It can be seen that a moderate electric field of about 10 kV/cm leads to a significant rearrangement of the spectrum (see Fig. 7). For the case of a strong electric field, the dependence on its orientation is significant [see Figs. 7(b) and 7(c)]. In particular, this dependence is most pronounced at energies around $30E_0$, where the interaction of the first, second, and third pairs of subbands leads to different anticrossing patterns.

A uniform electric field leads not only to an additional spin splitting of hole subbands, but also to a significant rearrangement of the wave function and a redistribution of the hole density (see Fig. 8). The hole density obviously is shifted in the electric field. The maps depicted in Fig. 8 have a quaint shape.

At first glance, the maps in Fig. 8 seem a bit asymmetric, which, for example, may be caused by insufficient accuracy of the numerical calculation. However, there is another reason for such a shape of the maps. The electric field **F** directed along the y axis ($\varphi_0 = \pi/2$) breaks the C_{3v} symmetry of the system. In this case the point symmetry is reduced to C_1, and there are no symmetry elements except for the identity one, $\boldsymbol{e}$. It seems there is the symmetry with respect to reflection in the vertical plane ($x = 0$). This is due to the predominance of the Rashba spin splitting over the Dresselhaus one. This symmetry will be restored if the BIA contributions are neglected. It should be noted that for the electric field **F** directed along the x axis ($\varphi_0 = 0$), the symmetry is partially conserved. In this case, the C_{3v} symmetry is reduced to the C_s one: One of the three symmetry planes is preserved, $(\bar{1}10)$.

Now TRS reflects the main symmetry properties of the subband spectrum and wave functions, since taking into account the BIA and the transverse electric field breaks the spatial inversion symmetry. The standard relation $E_\uparrow(k) = E_\downarrow(-k)$ remains valid. However, here the transition from spin $\uparrow$ to spin $\downarrow$ should be understood as the replacement of all projections of the hole spin by the opposite one, $J_z \to -J_z$. The corresponding envelope functions in this case are connected by complex conjugation. The latter means that the hole density maps for the time-reversed states coincide. The same is true for the separate HH and LH contributions.

V. DISCUSSION AND CONCLUSIONS

We start the discussion with a comparison of the results for the hole NW spectrum with and without inclusion in total

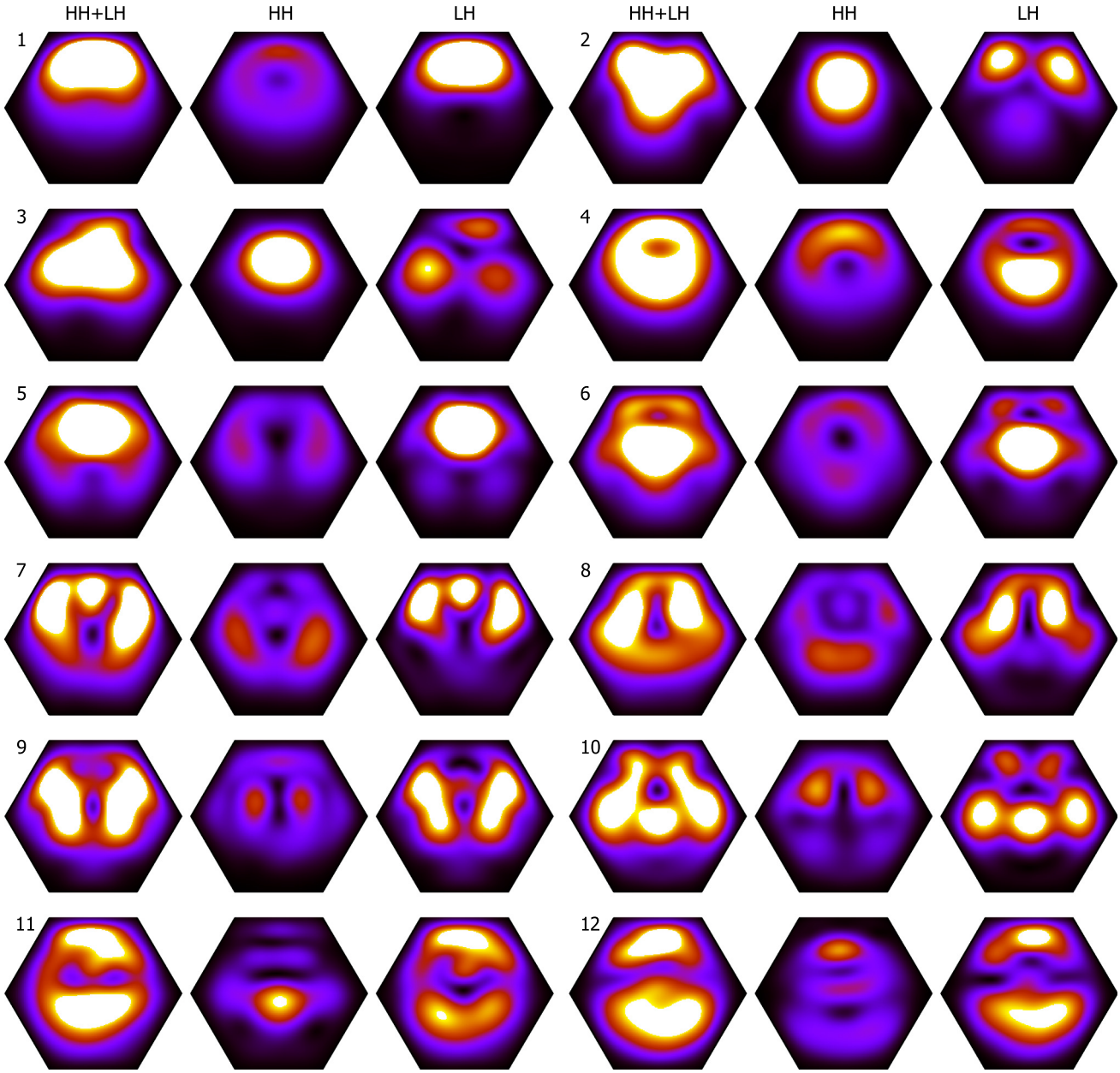

FIG. 8. The transverse hole density maps $|\Psi(r,\varphi)|^2$ for GaAs NW ($\gamma_1 = 6.85$, $\gamma_2 = 2.10$, $\gamma_3 = 2.90$) at $kR = 2.0$ in a transverse electric field $|e|FR/E_0 = 70$ directed perpendicular to the hexagon edge ($\varphi_0 = \pi/2$). The separate contributions for HH and LH are depicted. The maps are in arbitrary units, but all $|\Psi|^2$ are normalized to the same value. The subbands are numbered sequentially with increasing energy at given kR.

Hamiltonian BIA terms. The related issue of $\mathcal{H}_3^{[111]}$ matrix symmetrization is considered as well. The modification of the hole spectrum in WZ NWs is qualitatively considered.

A comparison of the results of Secs. III and IV shows that the inclusion of the BIA terms in the hole Hamiltonian is important and necessary. Accounting for the terms (11) and (13) leads to a significant rearrangement of the spectrum and wave functions. In some subbands, spin splitting takes place, while in others, a significant change in the shape of the spectrum occurs. The hole wave functions (or density distribution) are influenced by BIA contributions. The third-order rotational symmetry of the hole density map is restored due to BIA terms even at $k = 0$.

As mentioned above, the approach based on the 4×4 Luttinger Hamiltonian for calculating hole states in GaAs NWs is a good approximation. At the same time, it is necessary to take into account the real T_d symmetry of the material and include the corresponding BIA terms in the hole Hamiltonian. For NWs of narrow-gap III-V materials (InAs, InSb, etc.), it is necessary to take into account the exact interaction of the Γ_8 valence band with the Γ_6 conduction band and the Γ_7 split-off band, i.e., use multiband (six- or eight-band) calculations [73].

Nevertheless, the spin-orbit interaction is more pronounced in these materials than in GaAs. This means that the BIA terms should be included in the hole Hamiltonian all the more. Consistent accounting for the inversion asymmetry of the lattice for a narrow-gap material is possible within a 14-band model (the so-called extended Kane model), which explicitly considers higher conduction bands of Γ_7 and Γ_8 symmetry.

The Rashba spin splitting is important for the hole spectrum as well. The use of the real gate technique [70–72] leads to intricate distribution of the electric field and potential inside the NW. However, a significant rearrangement of the hole spectrum manifests itself even when a simple model with a uniform electric field is used. The distribution of the hole density is shifted by the electric field and has a quaint shape. Simultaneous accounting for the lack of an inversion center additionally reduces the symmetry of the problem.

The used simple procedure of forced symmetrization of the non-Hermitian operator of Eq. (13) is not strict and consistent. In the general case, one should start with a 14-band Hamiltonian, as was done by Durnev *et al.* [74] for quantum wells. On the other hand, there are a large number of examples when a simple symmetrization approach works. For example, the Hamiltonian for an electron in a thin quantum ring with Rashba spin-orbit splitting was first incorrectly derived in Ref. [75] and turned out to be non-Hermitian. The strict procedure for finding the correct operator is based on averaging of the high-dimensional Hamiltonian over the ground state wave function of the transverse motion [76,77]. However, a simple and fast procedure for forced symmetrization of a non-Hermitian operator also gives the same correct result. It should be noted that in this case, symmetrization at the level of differential operators is possible, and the Hamiltonian remains a 2×2 matrix with respect to the electron spin.

It should be remembered that NWs of GaAs under certain conditions can be crystalized in the WZ phase. In the first approximation, to describe hole states in WZ structures, it is necessary to introduce the influence of the crystal field into the Luttinger Hamiltonian. It is analogous to uniaxial strain, giving the splitting Δ_{cf} of HHs and LHs at $\mathbf{k} = 0$ [78]

$$\mathcal{H}_{cf} = -\frac{\Delta_{cf}}{2}\left(J_z^2 - \frac{5}{4}\right). \tag{16}$$

Accounting for this term leads to a significant change in the subband shape in Fig. 2. Moreover, the spin structure, namely the relation between HH and LH contributions, is changed dramatically. In WZ GaAs, the crystal field splitting Δ_{cf} is about 100 meV [79,80]. This means that accounting for $\mathcal{H}_{cf}$ in the total Hamiltonian leads to low-lying subbands that are of HH character (cf. with the results of Ref. [81]), which differs from the result in ZB NWs. Thus consideration of polytypic axial heterostructures may be of interest from the point of view of spintronics.

The strain can significantly renormalize the hole subband spectrum in NWs, especially taking into account the possible large elastic deformations in NWs compared with the bulk semiconductors. In the strained structure there are additional mechanisms of HH-LH mixing, which can introduce more complex terms into the hole Hamiltonian than, e.g., Eq. (16). However, this issue is beyond the scope of this paper and deserves separate consideration.

It should be noted that there is no direct possibility of constructing an effective Hamiltonian, say, for the first NW subband. For quantum wells, this problem is usually solved as follows: There is a solution for $k = 0$, and in the vicinity of this point the spectrum and the effective Hamiltonian are constructed perturbatively. Here we are faced with two difficulties: (i) The subband position at $k = 0$ cannot be found analytically, and (ii) even if the subband position found numerically is used, the constructed Hamiltonian will not make much sense, since at $k = 0$ the HH and LH states are already mixed. However, such a standard procedure can be useful for WZ NWs, where the ground and several excited subbands near $k = 0$ are predominantly of HH character and the LH contribution can be neglected.

In conclusion, the hole states in GaAs NWs with the [111] orientation and a hexagonal cross section are calculated. The necessity of taking into account in the Hamiltonian the terms that arise due to the lack of an inversion center in the ZB lattice is shown. This leads to a significant rearrangement of both the hole energy spectrum and the corresponding wave functions. The Rashba spin splitting of subbands due to the transverse electric field is also studied.

The used matrix approach with forced symmetrization of non-Hermitian terms is able to take into account all four issues that are important for NW states, as discussed in the Introduction. However, the strict procedure should be based on the extended Kane model, which explicitly takes into account the interaction with higher conduction bands and the corresponding splittings. The main advantage of our approach is the absence of nonphysical (rapidly oscillating) solutions, which usually appear when the problem is solved on the grid. It should be noted that it is possible to calculate the hole states in core-shell NWs generalizing an approach that we used for electrons in core-multishell NWs [82] with a cylindrical cross section.

ACKNOWLEDGMENTS

The author is grateful to N. S. Averkiev and A. M. Monakhov for useful discussions.

APPENDIX A: LUTTINGER HAMILTONIAN AND COORDINATE TRANSFORMATION

The invariant form of the Luttinger Hamiltonian is given by Eq. (1). Using the abovementioned representation of $J = 3/2$ matrices [46,47] and substituting their exact form into Eq. (1), we find the explicit form of the Luttinger Hamiltonian in the principal axes ($x||[100]$, $y||[010]$, $z||[001]$):

$$\mathcal{H}_L = \begin{pmatrix} P+Q & S & R & 0 \\ S^* & P-Q & 0 & R \\ R^* & 0 & P-Q & -S \\ 0 & R^* & -S^* & P+Q \end{pmatrix}, \tag{A1}$$

where $P = \frac{\hbar^2\gamma_1}{2m_0}(k_x^2 + k_y^2 + k_z^2)$, $Q = \frac{\hbar^2\gamma_2}{2m_0}(k_x^2 + k_y^2 - 2k_z^2)$, $S = -\frac{\sqrt{3}\hbar^2\gamma_3}{m_0}k_- k_z$, and $R = -\frac{\sqrt{3}\hbar^2}{2m_0}[\gamma_2(k_x^2 - k_y^2) - 2i\gamma_3 k_x k_y]$, with $k_\pm = k_x \pm ik_y$.

Here the coordinate transformation is presented, which is necessary to rewrite the Luttinger Hamiltonian in new axes ($x'||[11\bar{2}]$, $y'||[\bar{1}10]$, $z'||[111]$):

$$\begin{pmatrix} x \\ y \\ z \end{pmatrix} = \begin{pmatrix} \frac{1}{\sqrt{6}} & -\frac{1}{\sqrt{2}} & \frac{1}{\sqrt{3}} \\ \frac{1}{\sqrt{6}} & \frac{1}{\sqrt{2}} & \frac{1}{\sqrt{3}} \\ -\sqrt{\frac{2}{3}} & 0 & \frac{1}{\sqrt{3}} \end{pmatrix} \begin{pmatrix} x' \\ y' \\ z' \end{pmatrix}. \tag{A2}$$

Using this transformation for k_i and J_i ($i = x, y, z$) and substituting it into Eq. (1), we find the Hamiltonian (2). All BIA terms [Eqs. (11) and (13)] in the $(x'y'z')$ frame are obtained using the same transformation.

APPENDIX B: MATRIX ELEMENTS OF SOME OPERATORS

To calculate the matrix elements of the Hamiltonian between the functions (3), including the operators describing spin splittings, it is necessary to find the matrix elements of some combinations of $k_\pm$ operators between transverse envelopes $|mn\rangle$. For this purpose, it is convenient to use the well-known identity

$$k_\pm J_m(kr)e^{im\varphi} = \pm ikJ_{m\pm1}(kr)e^{i(m\pm1)\varphi}; \tag{B1}$$

after that, the calculation becomes trivial, taking into account the recurrence relations for the Bessel functions (see, for example, Ref. [83]) and the orthogonality of the basis functions. The matrix elements of the $k_\pm$ operators are given by

$$\langle m'n'|k_\pm|mn\rangle = \left(\frac{2i}{R}\right)\frac{j_{m'n'}j_{mn}}{j^2_{m'n'} - j^2_{mn}}\delta_{m',m\pm1}. \tag{B2}$$

It is easy to find the matrix elements of the operators $k^2_\pm$, which are given by

$$\langle m'n'|k^2_\pm|mn\rangle = \mp\left(\frac{2}{R}\right)^2\frac{(m\pm1)j_{m'n'}j_{mn}}{j^2_{m'n'} - j^2_{mn}}\delta_{m',m\pm2}. \tag{B3}$$

The particular case $\langle \pm1n|k^2_\pm|\mp1n\rangle$ requires separate consideration:

$$\langle \pm1n|k^2_\pm|\mp1n\rangle = \frac{j^2_{1n}}{R^2}. \tag{B4}$$

The matrix elements, which enter into Eq. (13), are given by

$$\langle m'n'|k^3_\pm|mn\rangle = -\frac{2i}{R^3}\frac{j_{m'n'}j_{mn}\left[4(m\pm2)(m\pm1) - j^2_{mn}\right]}{j^2_{m'n'} - j^2_{mn}}\delta_{m',m\pm3}, \tag{B5}$$

$$\langle m'n'|k_\pm k^2_\mp|mn\rangle = \frac{2i}{R^3}\frac{j_{m'n'}j^3_{mn}}{j^2_{m'n'} - j^2_{mn}}\delta_{m',m\mp1}. \tag{B6}$$

The non-Hermiticity of $k^3_\pm$ and $k_\pm k^2_\mp$ leads to the need for additional symmetrization of the matrix $\mathcal{H}^{[111]}_3$. The corresponding matrix elements are denoted as $\langle J'_z; m'n'; k|\mathcal{H}^{[111]}_3|J_z; mn; k\rangle_{\rm sym}$:

$$\begin{aligned}\langle 3/2; m'n'; k|\mathcal{H}^{[111]}_3|3/2; mn; k\rangle_{\rm sym} = &-\frac{\sqrt{3}b^{8v8v}_{41}}{4\sqrt{2}R^3}\frac{j_{m'n'}j_{mn}}{j^2_{m'n'} - j^2_{mn}}\Big\{\delta_{m',m+3}\left[8(m+1)(m+2) - j^2_{m'n'} - j^2_{mn}\right] \\ &- \delta_{m',m-3}\left[8(m-1)(m-2) - j^2_{m'n'} - j^2_{mn}\right]\Big\},\end{aligned} \tag{B7}$$

$$\begin{aligned}\langle 3/2; m'n'; k|\mathcal{H}^{[111]}_3|1/2; mn; k\rangle_{\rm sym} = &\frac{2b^{8v8v}_{41}}{R^3}\frac{j_{m'n'}j_{mn}}{j^2_{m'n'} - j^2_{mn}}\left[\frac{1}{8}\left(j^2_{m'n'} + j^2_{mn}\right) - (kR)^2\right]\delta_{m',m-1} \\ &- \frac{ib^{8v8v}_{41}\sqrt{2}k}{R^2}\frac{(m+1)j_{m'n'}j_{mn}}{j^2_{m'n'} - j^2_{mn}}\delta_{m',m+2}.\end{aligned} \tag{B8}$$

Other matrix elements can be derived using the properties of the $\mathcal{H}^{[111]}_3$ matrix (13). In the special case of $m' = 1$, $m = -1$, and $n' = n$ in accordance with Eq. (B4) the last term in the previous equation should be replaced by $(ikb^{8v8v}_{41}/2\sqrt{2}R^2)j^2_{1n}$.

The matrix element of the potential energy of the hole placed into a homogeneous electric field (15) between the transverse envelopes $|mn\rangle$ has the form

$$\langle m'n'|\mathcal{H}_F|mn\rangle = \frac{eFR(e^{-i\varphi_0}\delta_{m',m+1} + e^{i\varphi_0}\delta_{m',m-1})}{J_{|m'|+1}(j_{m'n'})J_{|m|+1}(j_{mn})}\int_0^1 dx x^2 J_{|m'|}(j_{m'n'}x)J_{|m|+1}(j_{mn}x) \tag{B9}$$

and requires numerical evaluation.

To calculate the overlap integral of basis functions (3), one needs at first to find the domain of integration. In Fig. 1(b) in the first shaded segment, this area in polar coordinates is defined as $0 \leqslant \varphi \leqslant \frac{\pi}{3}$ and $\frac{\sqrt{3}R}{\sqrt{3}\cos\varphi + \sin\varphi} \leqslant r \leqslant R$. After some simplifications, the overlap integral that enters the equation for the matrix element of the hexagonality potential (6) is given by

$$I_{m'n';mn} = \frac{1}{\pi J_{|m'|+1}(j_{m'n'})J_{|m|+1}(j_{mn})}\int_0^{\pi/3} d\varphi\cos(m-m')\varphi\int_{\frac{\sqrt{3}}{\sqrt{3}\cos\varphi+\sin\varphi}}^1 dx x J_{|m'|}(j_{m'n'}x)J_{|m|}(j_{mn}x) \tag{B10}$$

and can be evaluated numerically.

[1] C. Jia, Z. Lin, Y. Huang, and X. Duan, Nanowire electronics: From nanoscale to macroscale, Chem. Rev. **119**, 9074 (2019).

[2] S. A. Dayeh, D. P. Aplin, X. Zhou, P. K. Yu, E. Yu, and D. Wang, High electron mobility InAs nanowire field-effect transistors, Small **3**, 326 (2007).

[3] S. Chuang, Q. Gao, R. Kapadia, A. C. Ford, J. Guo, and A. Javey, Ballistic InAs nanowire transistors, Nano Lett. **13**, 555 (2013).

[4] X. Dai, S. Zhang, Z. Wang, G. Adamo, H. Liu, Y. Huang, C. Couteau, and C. Soci, GaAs/AlGaAs nanowire photodetector, Nano Lett. **14**, 2688 (2014).

[5] E. Barrigon, M. Heurlin, Z. Bi, B. Monemar, and L. Samuelson, Synthesis and applications of III-V nanowires, Chem. Rev. **119**, 9170 (2019).

[6] P. A. Alekseev, V. A. Sharov, P. Geydt, M. S. Dunaevskiy, V. V. Lysak, G. E. Cirlin, R. R. Reznik, A. I. Khrebtov, I. P. Soshnikov, and E. Lähderanta, Piezoelectric current generation in Wurtzite GaAs nanowires, Phys. Status Solidi RRL **12**, 1700358 (2018).

[7] R. Yan, D. Gargas, and P. Yang, Nanowire photonics, Nat. Photonics **3**, 569 (2009).

[8] N. I. Goktas, P. Wilson, A. Ghukasyan, D. Wagner, S. McNamee, and R. R. LaPierre, Nanowires for energy: A review, Appl. Phys. Rev. **5**, 041305 (2018).

[9] S. M. Frolov, S. R. Plissard, S. Nadj-Perge, L. P. Kouwenhoven, and E. P. A. M. Bakkers, Quantum computing based on semiconductor nanowires, MRS Bull. **38**, 809 (2013).

[10] V. S. Pribiag, S. Nadj-Perge, S. M. Frolov, J. W. G. van den Berg, I. van Weperen, S. R. Plissard, E. P. A. M. Bakkers, and L. P. Kouwenhoven, Electrical control of single hole spins in nanowire quantum dots, Nat. Nanotechnol. **8**, 170 (2013).

[11] H. Watzinger, J. Kukučka, L. Vukušić, F. Gao, T. Wang, F. Schäffler, J.-J. Zhang, and G. Katsaros, A germanium hole spin qubit, Nat. Commun. **9**, 3902 (2018).

[12] F. N. M. Froning, L. C. Camenzind, O. A. H. van der Molen, A. Li, E. P. A. M. Bakkers, D. M. Zumbühl, and F. R. Braakman, Ultrafast hole spin qubit with gate-tunable spin-orbit switch functionality, Nat. Nanotechnol. **16**, 308 (2021).

[13] S. Bosco, B. Hetényi, and D. Loss, Hole spin qubits in Si FinFETs with fully tunable spin-orbit coupling and sweet spots for charge noise, PRX Quantum **2**, 010348 (2021).

[14] S. Bosco and D. Loss, Hole spin qubits in thin curved quantum wells, Phys. Rev. Appl. **18**, 044038 (2022).

[15] O. Malkoc, P. Stano, and D. Loss, Charge-noise-induced dephasing in silicon hole-spin qubits, Phys. Rev. Lett. **129**, 247701 (2022).

[16] A. Bringer and Th. Schäpers, Spin precession and modulation in ballistic cylindrical nanowires due to the Rashba effect, Phys. Rev. B **83**, 115305 (2011).

[17] I. A. Kokurin, Determination of Rashba-coupling strength for surface two-dimensional electron gas in InAs nanowires, Solid State Commun. **195**, 49 (2014).

[18] I. A. Kokurin, Effect of spin-orbit coupling on spectral and transport properties of tubular electron gas in InAs nanowires, Phys. E (Amsterdam) **74**, 264 (2015).

[19] M. Kammermeier, P. Wenk, J. Schliemann, S. Heedt, and Th. Schäpers, Weak (anti)localization in tubular semiconductor nanowires with spin-orbit coupling, Phys. Rev. B **93**, 205306 (2016).

[20] P. Wójcik, A. Bertoni, and G. Goldoni, Tuning Rashba spin-orbit coupling in homogeneous semiconductor nanowires, Phys. Rev. B **97**, 165401 (2018).

[21] T. Campos, P. E. Faria Junior, M. Gmitra, G. M. Sipahi, and J. Fabian, Spin-orbit coupling effects in zinc-blende InSb and wurtzite InAs nanowires: Realistic calculations with multiband $\mathbf{k}\cdot\mathbf{p}$ method, Phys. Rev. B **97**, 245402 (2018).

[22] A. Bringer, S. Heedt, and Th. Schäpers, Dresselhaus spin-orbit coupling in [111]-oriented semiconductor nanowires, Phys. Rev. B **99**, 085437 (2019).

[23] P. Wójcik, A. Bertoni, and G. Goldoni, Enhanced Rashba spin-orbit coupling in core-shell nanowires by the interfacial effect, Appl. Phys. Lett. **114**, 073102 (2019).

[24] P. Wójcik, A. Bertoni, and G. Goldoni, Anisotropy of the spin-orbit coupling driven by a magnetic field in InAs nanowires, Phys. Rev. B **103**, 085434 (2021).

[25] M. J. Carballido, C. Kloeffel, D. M. Zumbühl, and D. Loss, Low-symmetry nanowire cross-sections for enhanced Dresselhaus spin-orbit interaction, Phys. Rev. B **103**, 195444 (2021).

[26] C. Kloeffel, M. Trif, and D. Loss, Strong spin-orbit interaction and helical hole states in Ge/Si nanowires, Phys. Rev. B **84**, 195314 (2011).

[27] C. Kloeffel, M. J. Rančić, and D. Loss, Direct Rashba spin-orbit interaction in Si and Ge nanowires with different growth directions, Phys. Rev. B **97**, 235422 (2018).

[28] C. Adelsberger, M. Benito, S. Bosco, J. Klinovaja, and D. Loss, Hole-spin qubits in Ge nanowire quantum dots: Interplay of orbital magnetic field, strain, and growth direction, Phys. Rev. B **105**, 075308 (2022).

[29] Yu. A. Bychkov and E. I. Rashba, Properties of a 2D electron gas with lifted spectral degeneracy, JETP Lett. **39**, 78 (1984).

[30] J.-W. Luo, S.-S. Li, and A. Zunger, Rapid transition of the hole Rashba effect from strong field dependence to saturation in semiconductor nanowires, Phys. Rev. Lett. **119**, 126401 (2017).

[31] G. Dresselhaus, Spin-orbit coupling effects in zinc blende structures, Phys. Rev. **100**, 580 (1955).

[32] J.-W. Luo, L. Zhang, and A. Zunger, Absence of intrinsic spin splitting in one-dimensional quantum wires of tetrahedral semiconductors, Phys. Rev. B **84**, 121303(R) (2011).

[33] D. Spirkoska, J. Arbiol, A. Gustafsson, S. Conesa-Boj, F. Glas, I. Zardo, M. Heigoldt, M. H. Gass, A. L. Bleloch, S. Estrade, M. Kaniber, J. Rossler, F. Peiro, J. R. Morante, G. Abstreiter, L. Samuelson, and A. Fontcuberta i Morral, Structural and optical properties of high quality zinc-blende/wurtzite GaAs nanowire heterostructures, Phys. Rev. B **80**, 245325 (2009).

[34] K. A. Dick, C. Thelander, L. Samuelson, and P. Caroff, Crystal phase engineering in single InAs nanowires, Nano Lett. **10**, 3494 (2010).

[35] J. Li and L.-W. Wang, Band-structure-corrected local density approximation study of semiconductor quantum dots and wires, Phys. Rev. B **72**, 125325 (2005).

[36] D. Karanth and H. Fu, Polarization ratio and effective mass in InP nanowires: Effect of crystallographic axis, Phys. Rev. B **74**, 155312 (2006).

[37] M. Luisier, A. Schenk, W. Fichtner, and G. Klimeck, Atomistic simulation of nanowires in the $sp^3d^5s^*$ tight-binding formalism: From boundary conditions to strain calculations, Phys. Rev. B **74**, 205323 (2006).

[38] Y. M. Niquet, A. Lherbier, N. H. Quang, M. V. Fernández-Serra, X. Blase, and C. Delerue, Electronic structure of semiconductor nanowires, Phys. Rev. B **73**, 165319 (2006).

[39] P. C. Sercel and K. J. Vahala, Analytical formalism for determining quantum-wire and quantum-dot band structure in the multiband envelope-function approximation, Phys. Rev. B **42**, 3690 (1990).

[40] H. Ando, S. Nojima, and H. Kanbe, Band-edge optical absorption spectra of GaAs quantum wires calculated by multiband effective mass theory, J. Appl. Phys. **74**, 6383 (1993).

[41] D. Csontos, P. Brusheim, U. Zülicke, and H. Q. Xu, Spin-$\frac{3}{2}$ physics of semiconductor hole nanowires: Valence-band mixing and tunable interplay between bulk-material and orbital bound-state spin splittings, Phys. Rev. B **79**, 155323 (2009).

[42] V. E. Degtyarev, S. V. Khazanova, and N. V. Demarina, Features of electron gas in InAs nanowires imposed by interplay between nanowire geometry, doping and surface states, Sci. Rep. **7**, 3411 (2017).

[43] A. Sitek, M. Urbaneja Torres, K. Torfason, V. Gudmundsson, A. Bertoni, and A. Manolescu, Excitons in core-shell nanowires with polygonal cross sections, Nano Lett. **18**, 2581 (2018).

[44] J. M. Luttinger, Quantum theory of cyclotron resonance in semiconductors: General theory, Phys. Rev. **102**, 1030 (1956).

[45] Strictly speaking, the Luttinger Hamiltonian is applicable for description of the valence band of semiconductors with the diamond crystal structure (point group O_h), such as Ge. However, as a first approximation, it is often used for materials with the ZB structure (point group T_d). The real T_d symmetry can be taken into account later, often by perturbation theory methods.

[46] E. L. Ivchenko and G. E. Pikus, *Superlattices and Other Heterostructures: Symmetry and Optical Phenomena*, 2nd ed. (Springer, Berlin, 1997).

[47] R. Winkler, *Spin-Orbit Coupling in Two-Dimensional Electron and Hole Systems* (Springer, Berlin, 2003).

[48] L. Wang and M. W. Wu, Hole spin relaxation in p-type (111) GaAs quantum wells, Phys. Rev. B **85**, 235308 (2012).

[49] I. A. Kokurin, Electronic states in nanowires with hexagonal cross-section, Semiconductors **54**, 1897 (2020).

[50] Here we will refer to states with $J_z = \pm 3/2$ and $J_z = \pm 1/2$ as HH and LH, respectively, as is accepted for quantum wells. At the same time, there is a significant difference between the quantization of holes in NWs and quantum wells. In the former case the quantization axis coincides with the direction of free motion, whereas in the latter case this is the direction of the quantum confinement. Moreover, in NWs the heavy and light states are already mixed at $k = 0$.

[51] A. Vezzosi, A. Bertoni, and G. Goldoni, Band structure of n- and p-doped core-shell nanowires, Phys. Rev. B **105**, 245303 (2022).

[52] The spin splitting associated with the interface inversion asymmetry (IIA) [84,85] is not mentioned here, since we consider a homogeneous NW. However, in the case of a core-shell structure this issue can be important.

[53] M. I. D'yakonov and V. I. Perel, Spin relaxation of conduction electrons in noncentrosymmetric semiconductors, Sov. Phys. Solid State **13**, 3023 (1972).

[54] M. I. D'yakonov and V. Yu. Kachorovskii, Spin relaxation of two-dimensional electrons in non-centrosymmetric semiconductors, Sov. Phys. Semicond. **20**, 110 (1986).

[55] E. L. Ivchenko and S. D. Ganichev, in *Spin Physics in Semiconductors* (Springer, New York, 2008), pp. 245–277.

[56] N. S. Averkiev and I. A. Kokurin, Current-induced spin orientation in semiconductors and low-dimensional structures, J. Magn. Magn. Mater. **440**, 157 (2017).

[57] G. E. Pikus, V. A. Marushchak, and A. N. Titkov, Spin splitting of energy bands and spin relaxation of carriers in cubic III-V crystals (Review), Sov. Phys. Semicond. **22**, 115 (1988).

[58] E. I. Rashba and E. Ya. Sherman, Spin-orbital band splitting in symmetric quantum wells, Phys. Lett. A **129**, 175 (1988).

[59] E. I. Rashba and V. I. Sheka, Combination resonance at acceptor centers, Sov. Phys. Solid State **6**, 451 (1964).

[60] G. L. Bir and G. E. Pikus, *Symmetry and Strain-Induced Effects in Semiconductors* (Wiley, New York, 1974).

[61] This procedure is not rigorous and cannot be justified within the model used. For verification, one can use the 14-band model (the so-called extended Kane model [47]), which explicitly takes into account these splittings. However, such a comparison is beyond the scope of this paper.

[62] M. Cardona, N. E. Christensen, and G. Fasol, Relativistic band structure and spin-orbit splitting of zinc-blende-type semiconductors, Phys. Rev. B **38**, 1806 (1988).

[63] E. I. Rashba and V. I. Sheka, Symmetry of energy bands in crystals of wurtzite type. II. Symmetry of bands with spin-orbit interaction included, Fiz. Tverd. Tela: Collect. Pap. **2**, 162 (1959).

[64] E. I. Rashba, Properties of semiconductors with an extremum loop. I. Cyclotron and comninational resonance in a magnetic field perpendicular to the plane of the loop, Sov. Phys. Solid State **2**, 1109 (1960).

[65] J. Nitta, T. Akazaki, H. Takayanagi, and T. Enoki, Gate control of spin-orbit interaction in an inverted $In_{0.53}Ga_{0.47}As/In_{0.52}Al_{0.48}As$ heterostructure, Phys. Rev. Lett. **78**, 1335 (1997).

[66] D. Liang and X. P. A. Gao, Strong tuning of Rashba spin-orbit interaction in single InAs nanowires, Nano Lett. **12**, 3263 (2012).

[67] Z. Scherübl, G. Fülöp, M. H. Madsen, J. Nygård, and S. Csonka, Electrical tuning of Rashba spin-orbit interaction in multigated InAs nanowires, Phys. Rev. B **94**, 035444 (2016).

[68] A. Iorio, M. Rocci, L. Bours, M. Carrega, V. Zannier, L. Sorba, S. Roddaro, F. Giazotto, and E. Strambini, Vectorial control of the spin-orbit interaction in suspended InAs nanowires, Nano Lett. **19**, 652 (2019).

[69] S. Datta and B. Das, Electronic analog of the electro-optic modulator, Appl. Phys. Lett. **56**, 665 (1990).

[70] K. Storm, G. Nylund, L. Samuelson, and A. P. Micolich, Realizing lateral wrap-gated nanowire FETs: Controlling gate length with chemistry rather than lithography, Nano Lett. **12**, 1 (2012).

[71] Q. Li, S. Huang, D. Pan, J. Wang, J. Zhao, and H. Q. Xu, Suspended InAs nanowire gate-all-around field-effect transistors, Appl. Phys. Lett. **105**, 113106 (2014).

[72] S. Morkötter, N. Jeon, D. Rudolph, B. Loitsch, D. Spirkoska, E. Hoffmann, M. Döblinger, S. Matich, J. J. Finley, L. J. Lauhon, G. Abstreiter, and G. Koblmüller, Demonstration of confined electron gas and steep-slope behavior in delta-doped GaAs-AlGaAs core-shell nanowire transistors, Nano Lett. **15**, 3295 (2015).

[73] N. Luo, G. Liao, and H. Q. Xu, k.p theory of freestanding narrow band gap semiconductor nanowires, AIP Adv. **6**, 125109 (2016).

[74] M. V. Durnev, M. M. Glazov, and E. L. Ivchenko, Spin-orbit splitting of valence subbands in semiconductor nanostructures, Phys. Rev. B **89**, 075430 (2014).

[75] A. G. Aronov and Y. B. Lyanda-Geller, Spin-orbit Berry phase in conducting rings, Phys. Rev. Lett. **70**, 343 (1993).

[76] A. V. Chaplik and L. I. Magarill, Effect of the spin-orbit interaction on persistent currents in quantum rings, Superlattices Microstruct. **18**, 321 (1995).

[77] F. E. Meijer, A. F. Morpurgo, and T. M. Klapwijk, One-dimensional ring in the presence of Rashba spin-orbit interaction: Derivation of the correct Hamiltonian, Phys. Rev. B **66**, 033107 (2002).

[78] Al. L. Efros, Luminescence polarization of CdSe microcrystals, Phys. Rev. B **46**, 7448 (1992).

[79] B. Ketterer, M. Heiss, E. Uccelli, J. Arbiol, and A. Fontcuberta i Morral, Untangling the electronic band structure of wurtzite GaAs nanowires by resonant Raman spectroscopy, ACS Nano **5**, 7585 (2011).

[80] N. Vainorius, S. Lehmann, A. Gustafsson, L. Samuelson, K. A. Dick, and M.-E. Pistol, Wurtzite GaAs quantum wires: One-dimensional subband formation, Nano Lett. **16**, 2774 (2016).

[81] S. Meier, P. E. Faria Junior, F. Haas, E.-S. Heller, F. Dirnberger, V. Zeller, T. Korn, J. Fabian, D. Bougeard, and C. Schüller, Intersubband excitations in ultrathin core-shell nanowires in the one-dimensional quantum limit probed by resonant inelastic light scattering, Phys. Rev. B **104**, 235307 (2021).

[82] A. O. Rudakov and I. A. Kokurin, Electronic states in cylindrical core-multi-shell nanowire, Semiconductors **53**, 2137 (2019).

[83] *Handbook of Mathematical Functions*, edited by M. Abramowitz and I. A. Stegun (Dover, New York, 1964).

[84] I. L. Aleiner and E. L. Ivchenko, Anisotropic exchange splitting in type-II GaAs/AlAs superlattices, JETP Lett. **55**, 692 (1992).

[85] E. L. Ivchenko, A. Yu. Kaminski, and U. Rössler, Heavy-light hole mixing at zinc-blende (001) interfaces under normal incidence, Phys. Rev. B **54**, 5852 (1996).